\$ SUPER

Contents lists available at ScienceDirect

Estuarine, Coastal and Shelf Science

journal homepage: www.elsevier.com/locate/ecss





Understanding the dynamic response of Durafet-based sensors: A case study from the Murderkill Estuary-Delaware Bay system (Delaware, USA)

S. Fisher Gonski ^{a,*}, William J. Ullman ^a, D. Tye Pettay ^b, Karl S. Booksh ^c, Todd R. Martz ^d, George W. Luther III ^a, Wei-Jun Cai ^{e,**}

- ^a School of Marine Science and Policy, University of Delaware, Lewes, DE, 19958, USA
- b Department of Natural Sciences, University of South Carolina Beaufort, Beaufort, SC, 29902, USA
- Department of Chemistry & Biochemistry, University of Delaware, Newark, DE, 19716, USA
- ^d Scripps Institution of Oceanography, University of California San Diego, La Jolla, CA, 92093, USA
- ^e School of Marine Science and Policy, University of Delaware, Newark, DE, 19716, USA

ARTICLE INFO

Keywords: pH ISFET Sensor Acidification Estuaries

ABSTRACT

The use of Durafet-based sensors has proliferated in recent years, but their performance in estuarine waters (salinity < 20) where rapid changes in temperature and salinity are frequently observed requires further scrutiny. Here, the responses of the Honeywell Durafet and its internal (pH^{INT}) and external (pH^{EXT}) reference electrodes integrated into a SeapHOx sensor at the confluence of the Murderkill Estuary and Delaware Bay (Delaware, USA) were assessed over extensive ranges of temperature (1.34-32.27°C), salinity (1.17-29.82), and rates of temperature $(dT/dt; -1.46 \text{ to } +1.53^{\circ}\text{C } (0.5 \text{ h})^{-1})$ and salinity $(dSalt/dt; -3.55 \text{ to } +11.09 (0.5 \text{ h})^{-1})$ change. Empirical analyses indicated dynamic errors in the temperature and salinity responses of the internal and external reference electrodes, respectively, driven by tidal mixing were introduced into our pH time-series. These dynamic errors drove large anomalies between pH^{INT} and pH^{EXT} (denoted $\Delta pH^{INT-EXT}$) that reached $>\pm 0.8$ pH in winter when the lowest temperatures and maximum tidal salinity variability occurred and >±0.15 pH in summer when the highest temperatures and minimum tidal salinity variability occurred. The $\Delta p H^{INT-EXT}$ anomalies demonstrated a clear linear relationship with dSalt/dt thereby making dSalt/dt the strongest limiting factor of reference electrode response in our application. A dynamic sensor response correction for the external reference electrode (solid-state chloiride ion-selective electrode, Cl-ISE) was also developed and applied in the voltage domain. This correction reduced winter and summer $\Delta pH^{INT-EXT}$ anomaly ranges by >40% and 68.7%, respectively. Summer anomalies were notably reduced to $<\pm0.04$ pH across all measurements. Further, this correction also removed the first-order salinity dependence of these anomalies. Consequently, dynamic errors in reference electrode response cannot be ignored and must be considered in future experimental designs. Further work to better understand the dynamic temperature and salinity responses of both reference electrodes is underway. Ultimately, we hope this work will stimulate further discussion around the role and treatment of large ΔpH^{INT-EXT} anomalies as a part of future data quality control and data reporting as well as the dynamic errors in reference electrode response that drive them in the context of Sensor Best Practices.

1. Introduction

Ocean acidification (OA) driven by oceanic absorption of anthropogenic carbon dioxide (CO_2) has driven pH decrease in the open ocean at rates ranging between -0.0026 and -0.0013 pH year⁻¹ (Bates et al., 2014). In biogeochemically active nearshore environments such as

estuaries, acidification or basification can occur at rates which are consistently an order of magnitude greater and range between -0.023 and +0.023 pH year⁻¹ (Carstensen and Duarte, 2019). Further, these contrasting pH trends are also often masked by substantial natural pH variability on tidal, diel, and monthly timescales that can reach >1 pH (Baumann et al., 2015; O'Boyle et al., 2013; Provoost et al., 2010).

E-mail addresses: sfgonski@udel.edu (S.F. Gonski), wcai@udel.edu (W.-J. Cai).

^{*} Corresponding author.

^{**} Corresponding author.

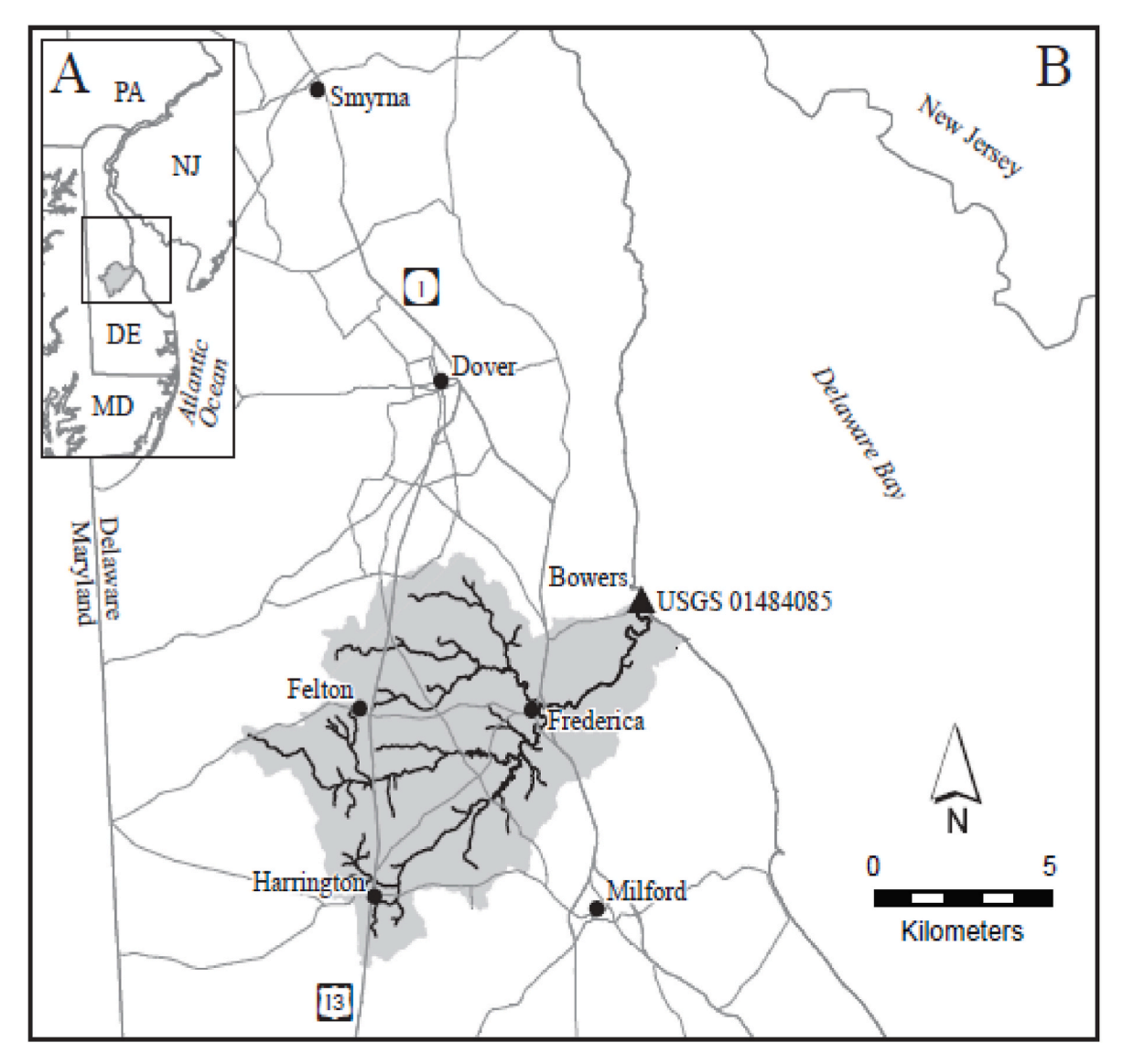


Fig. 1. Map of the Murderkill Estuary. The SeapHOx sensor deployment site was co-located with USGS Gauging Station 01484085 at the mouth of the Murderkill Estuary in Bowers, DE (USA).

Therefore, our ability to distinguish between long-term trends and natural variability and to determine controlling processes in estuaries hinges on accurately observing the marine CO_2 system through high-frequency pH measurements. In turn, this has led to intense scrutiny of the metrological challenges associated with pH measurement in natural waters (e.g., Dickson et al., 2016) which are further encumbered by the constant gradation of ionic strength in estuaries (Millero, 1986; Whitfield et al., 1985).

Over the past 40 years, potentiometric pH measurements in estuaries have been plagued by the same three challenges: (1) choice and characterization of an appropriate reference electrode (Butler et al., 1985; Culberson, 1981; Whitfield et al., 1985); (2) selection of standard buffers used to calibrate electrodes (Dickson, 1984; Easley and Byrne, 2012; Millero, 1986; Whitfield et al., 1985); and (3) absence of an accepted calibration strategy for pH measurements for natural waters ranging from freshwater to seawater (Butler et al., 1985; Dickson, 1984; Martz et al., 2015; Whitfield et al., 1985). Cai and Reimers (1993) also defined three requirements that all pH electrodes should satisfy on which performance can be evaluated: (1) quick response time; (2) consistent and stable voltage readings with low noise effects; and (3) the demonstration of close to 100% Nernstian response (e.g., -59.16 mV/pH at 25 °C).

In practice, the characterization and employment of a suitable

reference electrode is the primary metrological consideration for pH measurement in estuaries and supersedes the still notable discussion about the selection of standard buffers (Butler et al., 1985). Martell-Bonet and Byrne (2020) provides a full accounting of the buffer calibration method. Now, it is possible to calibrate a working autonomous pH sensor to the pH of discrete water samples collected alongside the sensor and measured using established benchtop methods (Hofmann et al., 2011). Recent work has demonstrated the extension of this straightforward calibration approach to estuaries (Gonski et al., 2018; Miller et al., 2021) which greatly simplifies the calibration strategy for future pH measurement in these settings. In recent years, the Honeywell Durafet (a hydrogen ion (H⁺)-selective Ion-Sensitive Field Effect Transistor (ISFET)) (Martz et al., 2010) has been used to measure marine and estuarine pH. The Honeywell Durafet satisfies all three pH electrode performance requirements defined by Cai and Reimers (1993) (Bagshaw et al., 2021; Long, 2021; Martz et al., 2010; Takeshita et al., 2014).

Together with its internal (Ag/AgCl reference) and a post-factory added external (solid-state chloride ion-selective electrode, Cl-ISE) reference electrodes, the modified version of the Durafet (commercially available from Sea-Bird Scientific (Bellevue, WA, USA)) has been integrated into autonomous sensor packages (e.g., SeaFET, SeapHOx, and Deep-Sea Durafet) and several mobile oceanographic monitoring

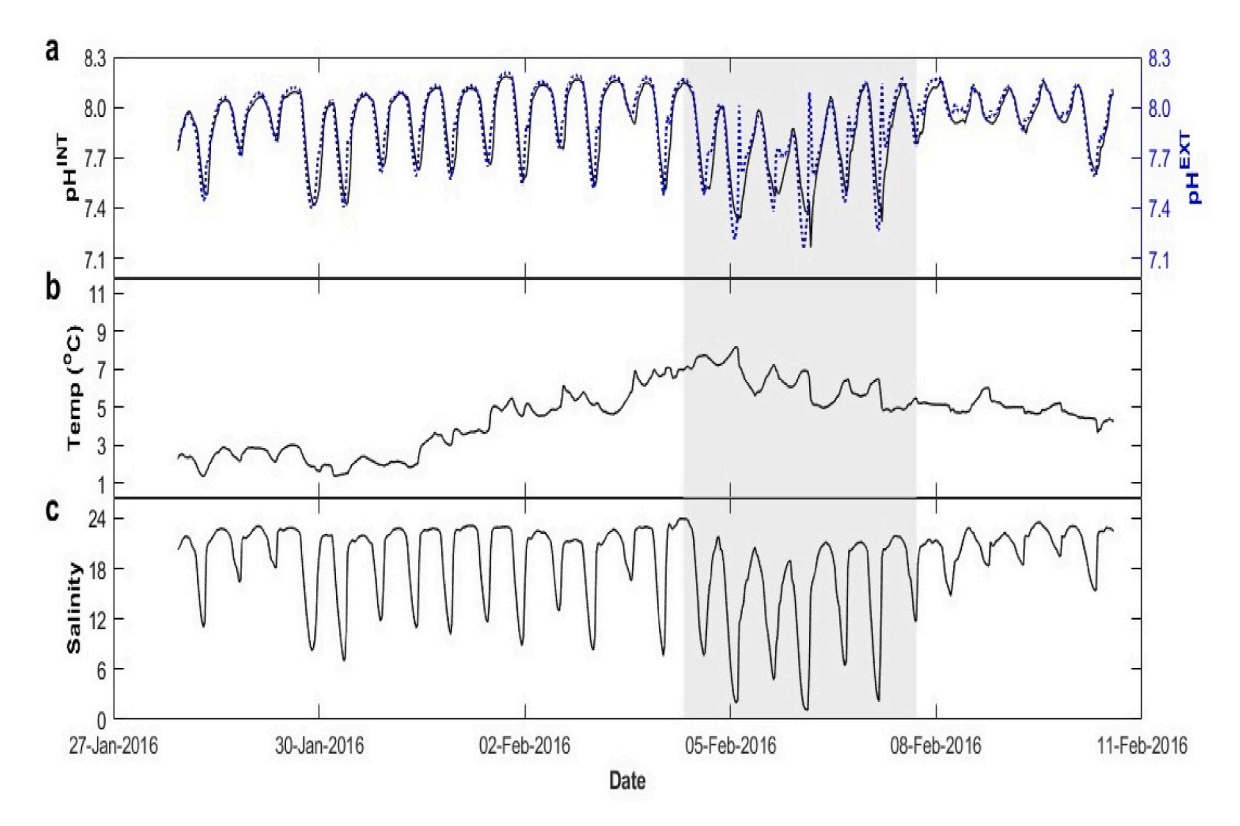


Fig. 2. Murderkill Estuary-Delaware Bay time-series between 27 January 2016 and 10 February 2016. Panel (a) shows the pH calculated using the internal (solid black) and external (dotted blue) reference electrodes. Panel (b) shows *in situ* temperature. Panel (c) shows salinity. The grey-shaded period between 04 February 2016 at 0730 and 08 February 2016 at 1700 highlights periods when upward and downward spikes in pH^{EXT} and pH^{INT}, respectively, are observed when slack ebb tide salinities repeatedly approach 1. pH data from the summer 2016 sensor deployment can be found in Fig. 3d of Gonski et al. (2018). (For interpretation of the references to color in this figure legend, the reader is referred to the Web version of this article.)

platforms whose use has proliferated in recent years (Bresnahan et al., 2014; Duke et al., 2021; Fritzsche et al., 2018; Johnson et al., 2016; Martz et al., 2010; Miller et al., 2018; Pettay et al., 2020; Shangguan et al., 2022). Despite this substantial body of work, a complete understanding of dynamic reference electrode response under rapid simultaneous changes in pH, temperature, and salinity has not been reported. As a result, there has been inconsistent reporting and use of pH measured with either the internal (pH^{INT}; Evans et al., 2019; Miller et al., 2018, 2021; Miller and Kelley, 2021, Rivest et al., 2016) or external (pH^{EXT}; Bresnahan et al., 2014, 2021; Takeshita et al., 2018) reference electrodes in different environments for various applications among sensor users.

Hence, there is a clear need for a more comprehensive evaluation of reference electrode response to identify and resolve dynamic errors in their temperature and salinity responses. Rather than using sensor data to detect a malfunctioning sensor as recommended (Bresnahan et al., 2014; Rivest et al., 2016), we, instead, work empirically to evaluate a working sensor. To do this, we use the consistently observed trends in anomalies between values of pHINT and pHEXT (denoted $\Delta pH^{INT-EXT}$) together with sensor voltages and other measured environmental data (e.g., temperature and salinity). We also propose and apply a dynamic sensor response correction to the voltage measured by the Cl-ISE. Herein, we report the results of a detailed assessment of internal and external reference response over extensive rates of pH, temperature, and salinity change performed using measurements made using a SeapHOx sensor package at the confluence of the Murderkill Estuary and Delaware Bay (Delaware, USA) collected during winter (27 January 2016 and 10 February 2016) and summer (20 July 2016 to 24 August 2016).

2. Materials & methods

The SeapHOx unit, SP053, used in the present study was originally assembled and tested at Scripps Institution of Oceanography. Accordingly, the equations describing the sensor's operating principle and practices associated with the sensor's functional implementation follow those presented in Bresnahan et al. (2014), Martz (2015), Martz et al. (2010), and Takeshita et al. (2014). The general performance of this same instrument was also evaluated in Gonski et al. (2018).

2.1. Sensor operation and its estuarine caveats

The Honeywell Durafet and its integrated reference electrodes calculate and report a pair of pH values on the total scale $(pH_T)\colon pH^{INT}$ (Ag/AgCl reference electrode containing a saturated KCl gel and diffusion liquid junction) and pH^{EXT} (non-porous solid-state chloride ion-selective electrode, Cl-ISE). Here, we briefly review reference electrode operation and pH calculation and outline any operational caveats applicable over wide ranges of pH, temperature, and salinity change in estuaries. Bresnahan et al. (2014) and Martz et al. (2010) discuss these topics further.

2.1.1. pH^{INT}

The internal reference of the Honeywell Durafet consists of an Ag wire surrounded by a saturated KCl gel which interfaces with the test solution through a liquid junction. pH^{INT} is calculated via:

$$pH^{INT} = \frac{\left(E_{INT} - E_{INT}^*\right)}{S},\tag{1}$$

where E_{INT} is the measured sensor voltage and E_{INT}^* is the calibration constant specific to the internal reference electrode (Martz et al., 2010).

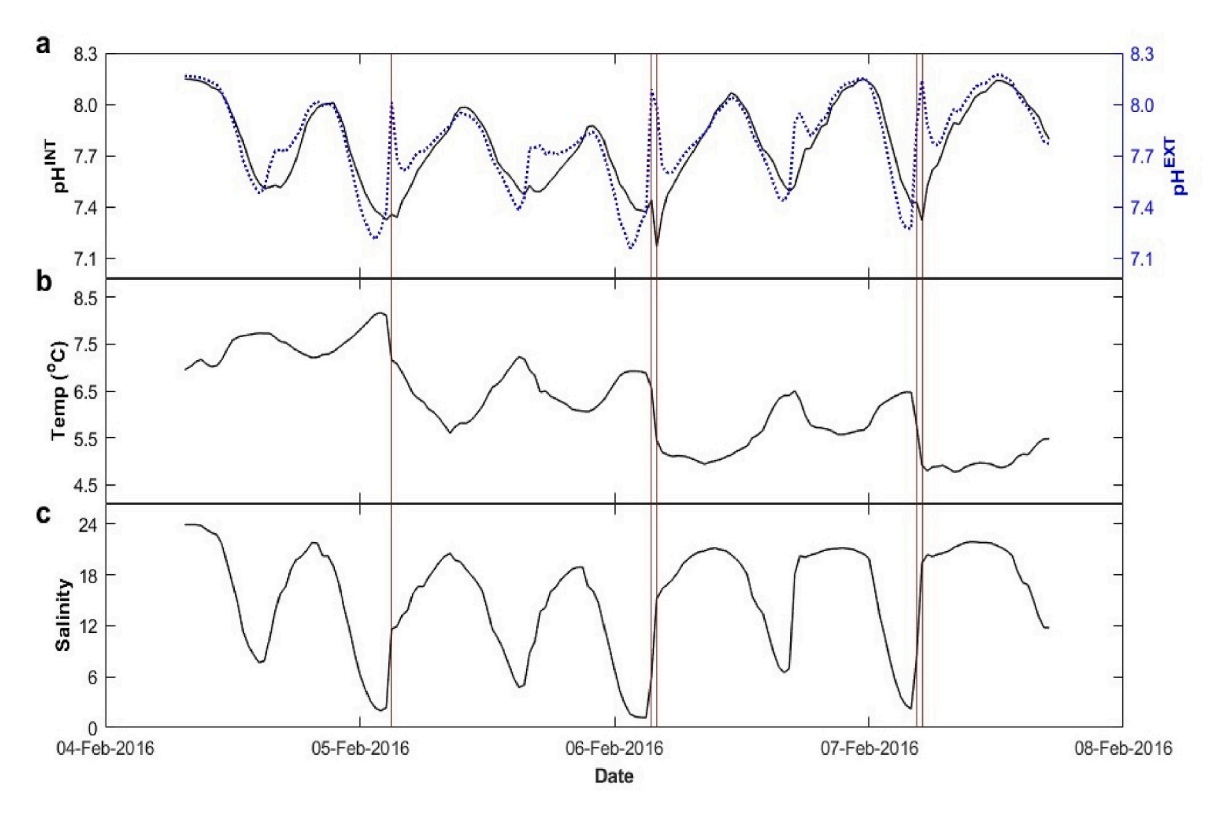


Fig. 3. Murderkill Estuary-Delaware Bay time-series between 04 February 2016 at 0730 and 08 February 2016 at 1700 (grey-shaded region in Fig. 2). Panel (a) shows the pH calculated using the internal (solid black) and external (dotted blue) reference electrodes. Panel (b) shows *in situ* temperature. Panel (c) shows salinity. Vertical red lines denote measurements on 05 February 2016 at 0300, 06 February 2016 at 0330 and 0400, and 7 February 2016 at 0430 and 0500 when upward and downward spikes in pH^{EXT} and pH^{INT}, respectively, align with flood tide measurements after tide reversal from slack ebb tide salinities that approach 1. (For interpretation of the references to color in this figure legend, the reader is referred to the Web version of this article.)

 \boldsymbol{S} is the temperature-dependent Nernst slope and is calculated via:

$$S = \frac{RT_K}{F} \times \ln(10), \tag{2}$$

where R is the gas constant (8.3145 J mol⁻¹K $^{-1}$), T_K is temperature in Kelvin, and F is the Faraday constant (96,485 C mol $^{-1}$) (Oldham et al., 2011). Using E_{INT} and *in situ* temperature, pH^{INT} is calculated assuming a 100% Nernst slope (*e.g.*, -59.16 mV/pH at 25°C) and a constant dE_{INT}^*/dT equal to -1.101 mV $^{\circ}$ C $^{-1}$ (Martz et al., 2010; Bresnahan et al., 2014).

The internal Ag/AgCl reference electrode contains a liquid junction so liquid junction potentials could impart systematic errors to $E_{\rm INT}$ measurements and subsequently calculated pH^{INT} (Bresnahan et al., 2014; Martz et al., 2010). Liquid junction potentials are functions of both temperature and ionic strength (calculated from salinity) so the internal reference electrode also possesses a salinity sensitivity (Bates, 1973). pH^{INT} errors due to liquid junction potentials could be problematic under rapid temperature variability and large salinity fluctuations (Bresnahan et al., 2014).

In estuaries with substantial temperature variability, additional thermal-induced errors can be introduced into pH^INT time-series if a thermal lag in the internal saturated KCl reference gel of the internal reference electrode occurs (Bresnahan et al., 2021). In other words, if the saturated KCl reference gel does not fully thermally equilibrate to the overlying water temperature during the measurement period, then the water temperature used to calculate the Nernst slope (T_K in equation (2)) and to correct E_{INT}^* between the reference temperature (e.g., 25°C in Bresnahan et al., 2014) and in situ temperature used to calculate pH^{INT} is not accurate.

2.1.2. **pH**^{EXT}

The Cl-ISE integrated with the Honeywell Durafet is nonporous solid

AgCl compressed into a solid pellet that uses the seawater chloride ion as the reference for its measurements (Martz et al., 2010). pH^{EXT} is calculated via:

$$pH^{EXT} = \frac{\left(E_{EXT} - E_{EXT}^*\right) + S \times \log(\gamma_H \gamma_{Cl} m_{Cl})}{S}, \tag{3}$$

where $E_{\rm EXT}$ is the measured sensor voltage and $E_{\rm EXT}^*$ is the calibration constant specific to external reference electrode (Cl-ISE), γ_i is the ion activity coefficient of either hydrogen (H⁺) or chloride (Cl⁻), $m_{\rm Cl}$ is the molality of Cl⁻, and S is the Nernst slope. pH^{EXT} is calculated assuming a 100% Nernst slope and a constant $dE_{\rm EXT}^*/dT$ of -1.048 mV $^{\rm O}C^{-1}$ from measured voltage, *in situ* temperature, and salinity. Unlike the internal reference, the Cl-ISE lacks a liquid junction and has a much smaller thermal mass (hence more rapid temperature equilibration relative to the internal reference). Since chloride ion activity in the ocean is a function of temperature and salinity, chloride ion concentrations (m_{Cl}) and ion activities ($\gamma_{\rm H}\gamma_{\rm Cl}$) also must be calculated to reflect variable environmental conditions to be included in the pH^{EXT} calculation (Martz et al., 2010).

Thus, m_{Cl} is calculated from salinity following Dickson et al. (2007), and ion activities are calculated from temperature between 5 and 40°C and salinity between 20 and 45 using the empirical function for the mean activity coefficient of HCl ($\gamma_{\pm HCl}$) reported by Khoo et al. (1977). Accordingly, the Cl-ISE and pH EXT are inherently salinity-dependent (Martz et al., 2010). Any further inaccuracies associated with m_{Cl} and $\gamma_{\pm HCl}$ calculations at salinities outside of their valid published temperature and salinity ranges will impart errors to pH EXT time-series.

Upstream discharge of highly chlorinated water or wastewater treatment plant effluent into estuarine or coastal waters where sensors are deployed may also increase ratios of chloride ion concentration to

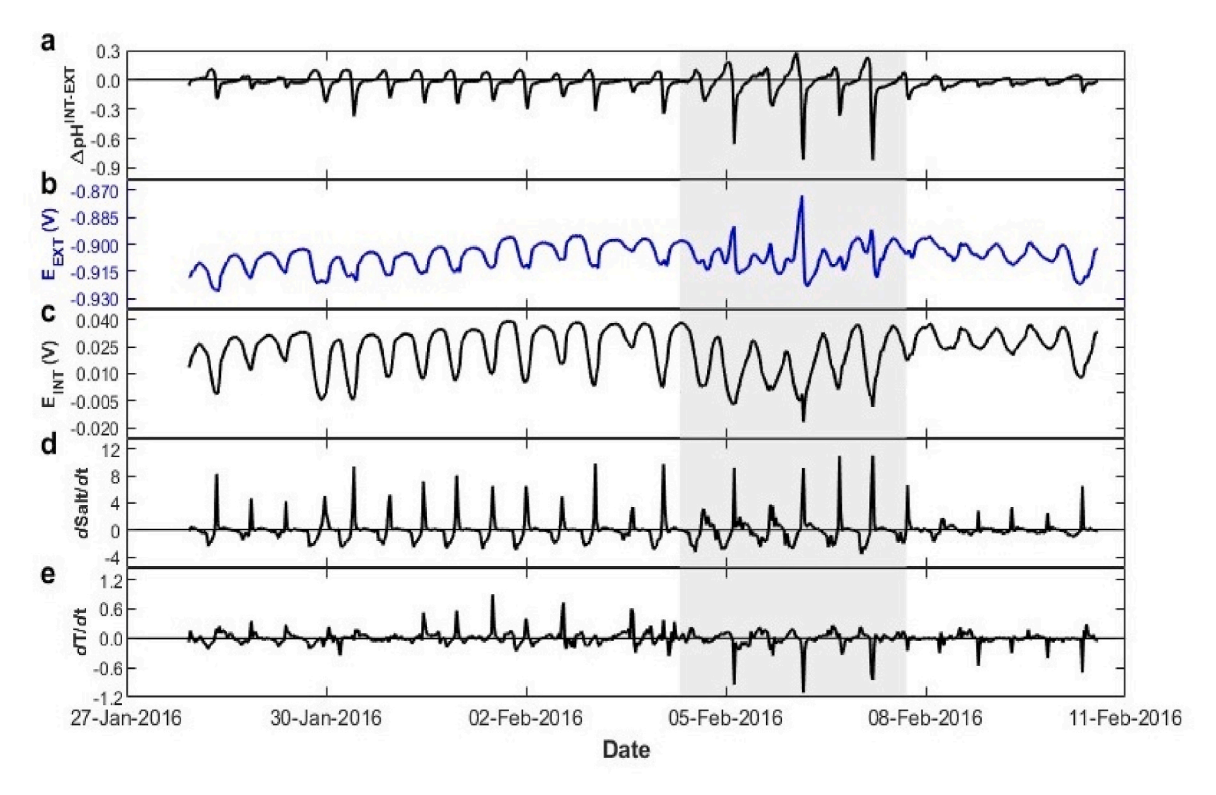


Fig. 4. Murderkill Estuary-Delaware Bay pH anomaly time-series between 27 January 2016 and 10 February 2016. Panel (a) shows the Δ pH^{INT}-EXT anomalies relative to a zero anomaly (solid black line). Panels (b) and (c) show the voltages measured using the external (blue) and internal (black) reference electrodes, respectively. Panel (d) shows the rate of change in salinity (dSalt/dt, (0.5 h)⁻¹) relative to a zero change (solid black line). Panel (e) shows the rate of change in *in situ* temperature (dT/dt, $^{\circ}$ C (0.5 h)⁻¹) relative to a zero change (solid black line). The grey-shaded period between 04 February 2016 at 0730 and 08 February 2016 at 1700 highlights periods when slack ebb tide salinities approach 1 (also shown in Figs. 2 and 3) coincide with the largest Δ pH^{INT}-EXT anomalies, upward spikes in E_{EXT} and downward spikes in E_{INT} (same direction as the pH spikes), and the most extreme positive dSalt/dt and most extreme negative dT/dt on flood tides after tide reversal. (For interpretation of the references to color in this figure legend, the reader is referred to the Web version of this article.)

salinity relative to those in seawater at salinities ≤ 5 and impact Cl-ISE response. Still further, Cl-ISE response may be complicated by environmental chloride ion $[CI^-]$ and anion $[X^-]$ concentrations and prevailing chloride-to-anion ratios $(CI^-:X^-)$. This results from the Cl-ISE's cross-sensitivity to interfering anions including bromide (Br^-) , iodide (I^-) , sulfate (SO_4^{2-}) , and sulfide (S^{2-}) due to equilibrium with AgCl (Bard et al., 1985). This imparts an additional salinity dependence to the Cl-ISE (Gonski et al., 2018; Takeshita et al., 2014).

2.2. Cl-ISE dynamic sensor response correction

Equation (3) for pHEXT is governed by the complete cell reaction of:

$$AgCl + \frac{1}{2} H_2 \rightarrow Ag^+ + H^+ + Cl^-, \tag{4}$$

where the electrode couple consisting of the Cl-ISE (reference electrode) and Durafet (H⁺-sensitive measuring electrode) measures dissolved hydrogen chloride (HCl) directly in the sample; this is expressed through $E_{\rm EXT}$ (Martz et al., 2010). This electrochemical response is parameterized as the activity product of hydrogen and chloride $(a_{\rm H}a_{\rm Cl})$ for the purposes of pH $^{\rm EXT}$ calculation using equation (3). To produce the log term in the second half of equation (3), $a_{\rm H}a_{\rm Cl}$ is further reduced via:

$$log_{10}(a_{H}a_{Cl}) = log_{10}(\gamma_{H}\gamma_{Cl}) + log_{10}(m_{H}m_{Cl}) = log_{10}(\gamma_{H}\gamma_{Cl}m_{Cl}) - pH, \tag{5} \label{eq:5}$$

where $log_{10}(m_H)$ equates to pH and gets moved to the opposite side of equation (3) (Bresnahan et al., 2021).

However, if we consider the reference electrode half-cell response of the Cl-ISE (designated ISE) separately, the accompanying half reaction for the Cl-ISE is:

$$AgCl + e^{-} \rightarrow Ag^{+} + Cl^{-}, \tag{6}$$

which has the following Nernst equation:

$$E_{ISE} = E_{ISE}^{o} - S \times \log(a_{CI}) = E_{ISE}^{o} - S \times \log(\gamma_{CI} m_{CI}), \tag{7}$$

where E_{ISE} is the measured voltage for the AgCl electrode that is incorporated into E_{EXT} and E_{ISE}^{o} is the electrode standard potential that is incorporated into E_{EXT}^* from equation (3). On this basis, the Cl-ISE only exhibits a Nernstian response to a_{Cl} (and salinity) that is expressed through its measured voltage (E_{ISE}) and not to a_{H} or pH.

On its own, E_{ISE} exhibits an inverse relationship with a^{CI} and salinity meaning that E_{ISE} increases as a_{CI} and salinity decrease and vice versa. From this, a temporal change in E_{ISE} $\left(\frac{dE_{ISE}}{dt}\right)$ isolated to the voltage contribution of a_{CI} can be calculated via:

$$\frac{d\mathbf{E}_{\text{ISE}}}{dt} = \frac{\left(\left[\mathbf{E}_{\text{ISE}}^{\text{o}} - \mathbf{S} \times \log(\gamma_{\text{CI}} \mathbf{m}_{\text{CI}}) \right]_{f} - \left[\mathbf{E}_{\text{ISE}}^{\text{o}} - \mathbf{S} \times \log(\gamma_{\text{CI}} \mathbf{m}_{\text{CI}}) \right]_{i} \right)}{dt},$$
(8)

and equation (8) can then be further reduced after subtracting out redundant $E_{\rm ISE}^{\rm o}$ to:

$$\frac{dE_{ISE}}{dt} = \frac{\left(\left[-S \times \log(\gamma_{CI} m_{CI})\right]_f - \left[-S \times \log(\gamma_{CI} m_{CI})\right]_i\right)}{dt},$$
(9)

where the quantities denoted subscript f and i are the final and initial values for each time step.

On this basis, we propose a pH-independent dynamic sensor response correction applied to $E_{\rm EXT}$. It corrects the salinity response of the Cl-ISE to new salinities by imitating the inverse relationship between $E_{\rm ISE}$ and

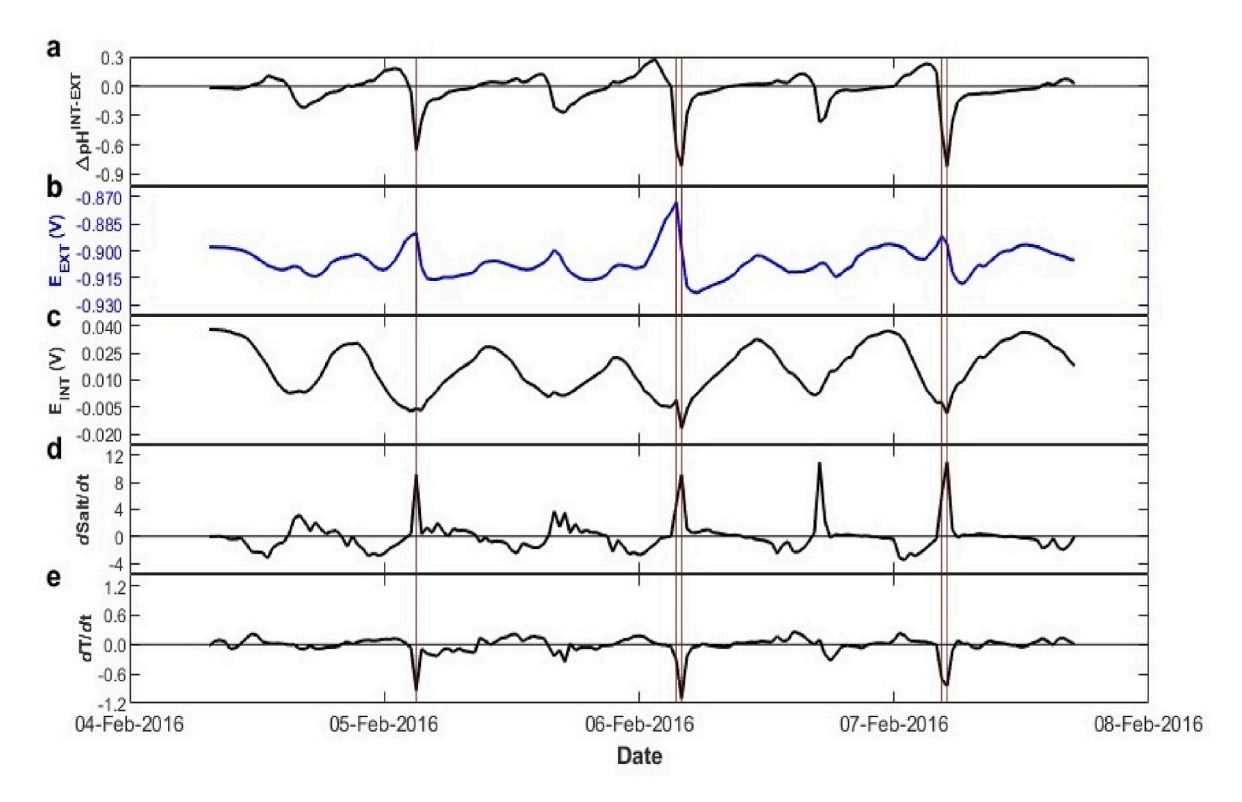


Fig. 5. Murderkill Estuary-Delaware Bay pH anomaly time-series between 04 February 2016 at 0730 and 08 February 2016 at 1700 (grey-shaded region in Fig. 4). Panel (a) shows the Δ pH^{INT-EXT} anomalies relative to a zero anomaly (solid black line). Panels (b) and (c) show the voltages measured using the external (blue) and internal (black) reference electrodes, respectively. Panel (d) shows the rate of change in salinity (dSalt/dt, (0.5 h)⁻¹) relative to a zero change (solid black line). Panel (e) shows the rate of change in *in situ* temperature (dT/dt, ${}^{\circ}$ C (0.5 h)⁻¹) relative to a zero change (solid black line). Vertical red lines denote measurements on 05 February 2016 at 0300, 06 February 2016 at 0330 and 0400, and 07 February 2016 at 0430 and 0500 when the largest Δ pH^{INT-EXT} anomalies, upward spikes in E_{EXT} and downward spikes in E_{INT} (same direction as the pH spikes), and the most extreme positive dSalt/dt and most extreme negative dT/dt align with flood tide measurements after tide reversal from slack ebb tide salinities that approach 1. (For interpretation of the references to color in this figure legend, the reader is referred to the Web version of this article.)

 a_{Cl} (and salinity). In other words, the correction compensates for the salinity response by making E_{EXT} more positive as a_{Cl} and salinity decrease and vice versa. The equation for the correction is equivalent to equation (3) for pH^{EXT} , but E_{EXT} is modified to E_{EXT}^{corr} . E_{EXT}^{corr} is linear with time and is calculated via:

$$E_{\rm EXT}^{\rm corr} = E_{\rm EXT}^{\rm meas} + (\tau_{\rm E_{ISE}}) \left(\frac{dE_{\rm ISE}}{dt} \right), \tag{10}$$

where E_{EXT}^{meas} is the measured E_{EXT} , au_{EISE} is a time constant for E_{ISE} in units of time, and $\frac{dE_{ISE}}{dt}$ is rate of the change in E_{ISE} in units of V time⁻¹.

Since Cl-ISE response is fully Nernstian (Takeshita et al., 2014), $\frac{dE_{ISE}}{dt}$ is expressed through the term, $\log(\gamma_H\gamma_{Cl}m_{Cl})$, and is calculated using the form of equation (9) via:

$$\frac{dE_{ISE}}{dt} = \frac{\left(\left[-S \times \log(\gamma_{H}\gamma_{CI}m_{CI})\right]_{f} - \left[-S \times \log(\gamma_{H}\gamma_{CI}m_{CI})\right]_{i}\right)}{1800 \text{ sec}}$$
(11)

where S remains the temperature-dependent Nernst slope. The $\log(\gamma_{\rm H}\gamma_{\rm Cl}m_{\rm Cl})$ terms in the quantities denoted subscript f and i are the final and initial values for each time step. They are calculated from temperature and salinity measured by the SBE37 conductivity-temperature sensor during the final (or current) (f) and initial (or previous) (i) sampling cycles, respectively, for measurements occurring every 1800 sec (or 30 min). The inclusion of $\gamma_{\rm H}$ in $\frac{dE_{\rm ISE}}{dt}$ arises since $\gamma_{\rm H}\gamma_{\rm Cl}$ must be calculated together according to Khoo et al. (1977) using equation (3) based on the complete cell reaction. In equation (3) for pH^{EXT}, $[-S \times \log(\gamma_{\rm H}\gamma_{\rm Cl}m_{\rm Cl})]_f$ is used and terms are calculated using temperature and salinity measured during the final (or current)

sampling cycle

The dynamic sensor response correction for the Cl-ISE potentially accounts for the following either singly or in combination – (1) the slow replacement of Cl^- with other anions like Br^- on the surface of the AgCl solid element as salinity changes, (2) equilibration issues due to a thermal lag in Cl-ISE response as temperature changes, and (3) flow housing carryover caused by an incomplete flushing of the flow housing where the waters measured by the electrodes are a combination of "old" water from the previous sampling cycle and "new" water from the current sampling cycle that would result in different salinities being measured by the SBE37 conductivity-temperature sensor and seen by the electrodes in the flow housing.

We use a $\tau_{E_{ISE}}$ equal to our sampling interval of 1800 sec. We assume $\tau_{E_{ISE}}$ is the maximum amount of time the CI-ISE would need to fully respond to the new salinities and is similar to the sampling interval rather than the much quicker pump times (50 or 70 sec; Table S1) used to renew the water inside the flow housing where the electrodes are located. The impacts of the dynamic sensor response correction for the CI-ISE on the $\Delta pH^{INT-EXT}$ anomalies that support these assumptions are discussed in section 3.2.3 and in the Supplementary Materials.

2.3. Field deployment

The SeapHOx sensor package includes sensors for temperature and salinity (reported on the Practical Salinity Scale, PSS-78) (Sea-Bird Electronics Conductivity-Temperature Sensor – SBE37), pH (Honeywell Durafet), and dissolved oxygen (Aanderaa Data Instruments 4835 Optode) plumbed into a flow path that is flushed by a Sea-Bird Electronics (SBE) 5M submersible pump (Bresnahan et al., 2014).

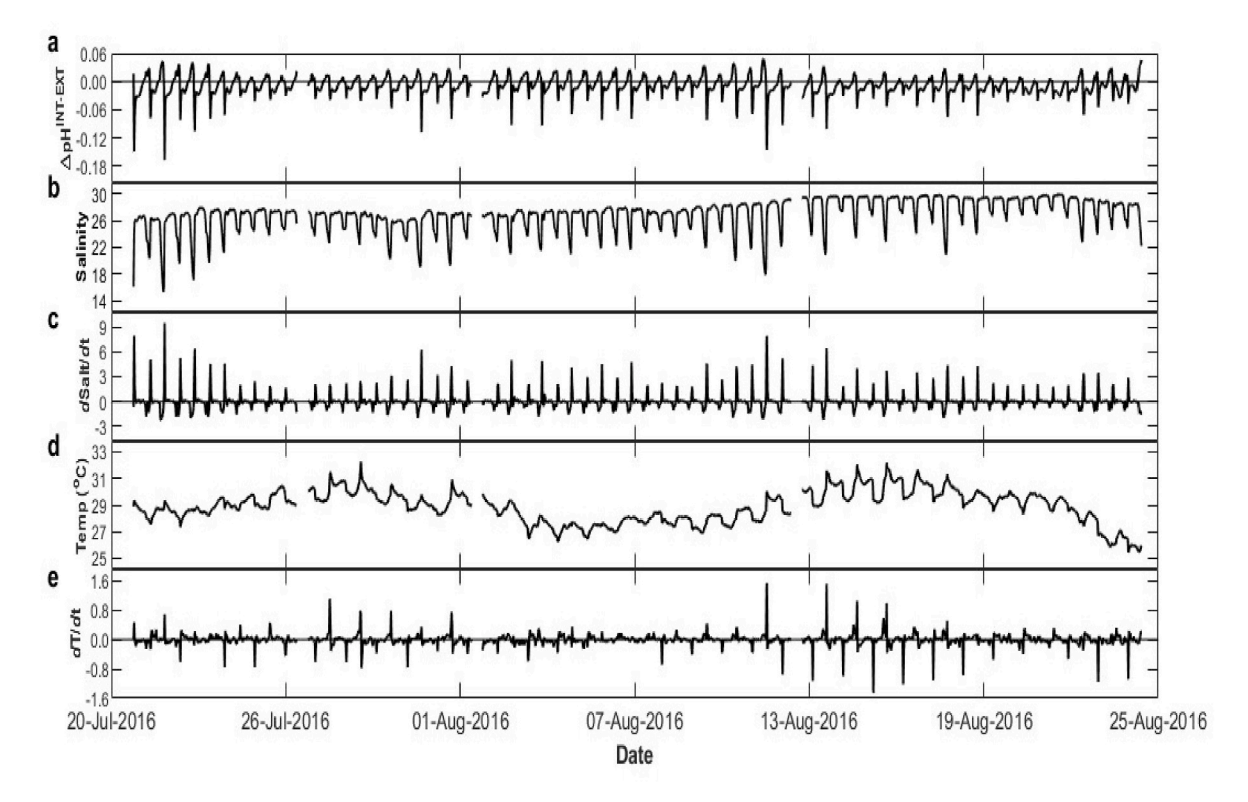


Fig. 6. Murderkill Estuary-Delaware Bay pH anomaly time-series between 20 July 2016 to 24 August 2016. Panel (a) shows the Δ pH^{INT-EXT} anomalies shown relative to a zero anomaly. Panel (b) shows salinity. Panel (c) shows the rate of change in salinity (dSalt/dt, (0.5 h)⁻¹) relative to a zero change. Panel (d) shows temperature ($^{\circ}$ C). Panel (e) shows the rate of change in *in situ* temperature (dT/dt, $^{\circ}$ C (0.5 h)⁻¹) relative to a zero change. Gaps in the data represent sensor maintenance and proceeding 6-h intra-deployment conditioning periods.

One SeapHOx unit (SP053) that was configured to measure every 30 min was deployed in two different sensor flow configurations better suited to our specific application: Configuration v2.0 between 11 December 2015 and 04 April 2016 and Configuration v3.0 between 20 July 2016 and 24 August 2016 (Table S1 and Fig. S1). Pump times and pH sample averages incorporated into sensor deployment configurations at different times (Table S1) were varied to design a set of experiments to assess reference electrode response under dynamic conditions. For more details about the sensor deployment configurations, sample collection and analytical methods, and sensor calibration, please see the Supplementary Materials.

2.4. Study site

SP053 was deployed at Bowers, Delaware (Lat. 39.05°N, Lon. 75.39°W) at the confluence of the Murderkill Estuary and Delaware Bay. In the flood-dominant, tidally-forced Murderkill Estuary-Delaware Bay System (Dzwonkowski et al., 2013), the two dominant endmembers are the fresher Murderkill Estuary outflow and more saline Delaware Bay Water. Due to its substantially smaller mean channel width and depth and smaller water volume relative to Delaware Bay, the Murderkill Estuary outflow experiences more thermal variability during day/night and periods of unseasonably warmer or cooler air temperatures than the more thermally stable Delaware Bay. Because of this, the fresher Estuary outflow can be warmer or cooler than the more saline Delaware Bay water throughout the year (Ullman et al., 2013; Voynova et al., 2015).

The lowest salinities coincide with the lowest pH during slack ebb tides which reflect the largest contributions from the Murderkill Estuary outflow (Gonski et al., 2018; Ullman et al., 2013) usually coinciding with the largest freshwater flows (Voynova et al., 2015). Environmental drivers of local biogeochemistry include high-frequency tidal fluctuations and low-frequency subtidal controls of winds, large storms, and

spring-neap tides (Dzwonkowski et al., 2013; Voynova et al., 2015; Wong et al., 2009). Because of this, tidal pH fluctuations largely follow tidal salinity fluctuations.

3. Results and discussions

In the Murderkill Estuary-Delaware Bay System, winter and summer represent opposing environmental extremes. The lowest water temperatures and maximum tidal salinity variability are observed in winter while the highest water temperatures and minimum tidal salinity variability are observed in summer. We use sensor data collected in winter between 27 January 2016 and 10 February 2016 and summer between 20 July 2016 and 24 August 2016 (originally published in Gonski et al. (2018)) to represent these seasonal environmental extremes.

3.1. General electrode response

In winter, sensor pH measurements (Fig. 2a) calculated from the measured voltages generally exhibit good agreement across the natural wide range of lower temperatures (Fig. 2b) and lower salinities (Fig. 2c). Diel pH fluctuations of >0.5 pH units were characterized by better alignment of pH^{INT} and pH^{EXT} during high tide, but then the two values diverged between the end of slack ebb tide and the beginning of the next flood tide. The divergence between the two pH values was most prominent between 04 February 2016 and 08 February 2016 (grey highlighted region in Fig. 2 and Fig. 3) when sharp upward and downward spikes in pH^{EXT} and pH^{INT}, respectively (indicated by vertical red lines in Fig. 3a), were observed coinciding with salinities that reached 1 at the end of slack ebb tide before tide reversal (Fig. 3c). During summer, pH^{INT} and pH^{EXT} are generally devoid of any substantial divergence across its respective ranges of pH, temperature, and salinity (please see Fig. 3d–fin Gonski et al. (2018)). For comparisons of winter sensor pH and

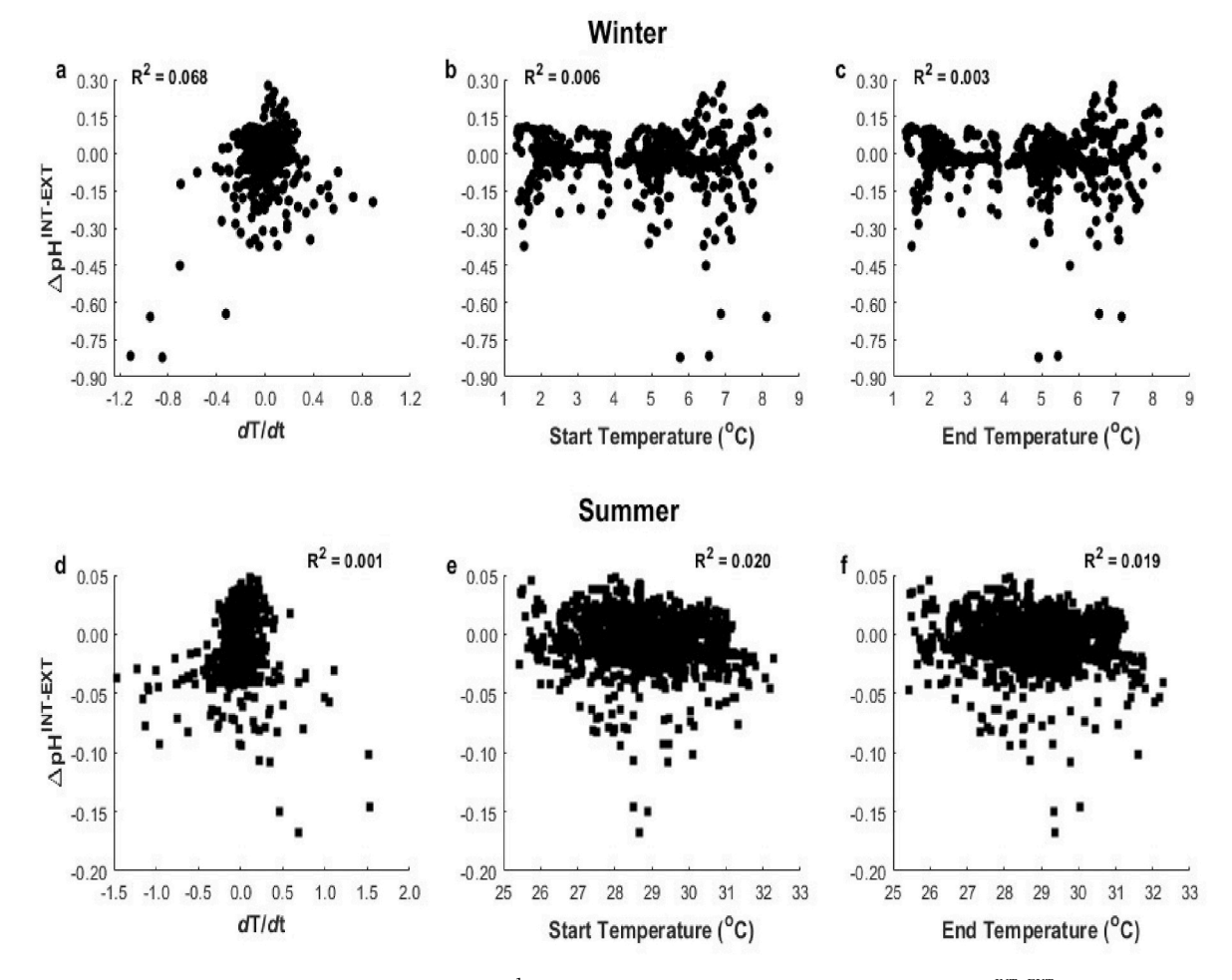


Fig. 7. Effect of the rate of change in temperature $(dT/dt, {}^{\circ}C (0.5 h)^{-1})$, starting temperature, and ending temperature on $\Delta pH^{INT-EXT}$ anomalies during (a–c) winter between 27 January 2016 and 10 February 2016 (circles) and (d–f) summer between 20 July 2016 and 24 August 2016 (squares). Start and end temperatures represent the initial and final temperatures for each time step recorded by the SBE37 conductivity-temperature sensor on the previous and current sampling cycles, respectively, performed every 30 min. dT/dt is the difference between them.

discrete sample pH, please see Fig. S3 in the Supplementary Materials.

3.2. Assessment of dynamic electrode response

A typical assessment of sensor performance to detect effects of biofouling or sensor failure involves direct comparisons of the non-zero anomalies between pH^{INT} and pH^{EXT} (Δ pH^{INT}-EXT) (e.g., Bresnahan et al. (2014) and Rivest et al. (2016)). In addition, we found it useful in this study to further examine the raw sensor voltages measured by the internal (E_{INT}) and external (E_{EXT}) reference electrodes.

3.2.1. Seasonal data comparison

Under opposing seasonal environmental extremes, short-lived, transient $\Delta p H^{INT-EXT}$ anomalies that approached ± 0.85 pH were consistently observed. In winter, the evolution of larger $\Delta p H^{INT-EXT}$ anomalies (Fig. 4a) generally followed tidal trends. A positive $\Delta p H^{INT-EXT}$ anomaly $(p H^{INT} > p H^{EXT})$ persists over prolonged periods of salinity decrease on the ebb tide. On ebb tides, rates of salinity change (dSalt/dt, Fig. 4d) are negative and relatively smaller compared to the flood tides (\leq –4 (0.5 h) $^{-1}$). Maximum $\Delta p H^{INT-EXT}$ anomalies are generally reached when salinity reached its minimum at slack ebb tide reflecting the greatest influence of the fresher Murderkill Estuary outflow. This is followed by a sharp rapid decrease to a negative $\Delta p H^{INT-EXT}$ anomaly (pH INT < pH EXT) coinciding with tide reversal when the greatest positive dSalt/dt (\leq +11 (0.5 h) $^{-1}$) was observed on

the flood tide. Finally, a near-zero $\Delta p H^{INT-EXT}$ anomaly was reached once the more saline Delaware Bay water inundates the sensor deployment site, environmental conditions stabilize, and rates of salinity change approach zero. The resulting asymmetric trends in the $\Delta p H^{INT-EXT}$ anomalies are driven by the discharge asymmetry in our system with slow pH changes on ebb tides and more rapid pH changes on flood tides (Dzwonkowski et al., 2013). Periods with the greatest observed $\Delta p H^{INT-EXT}$ anomalies are indicated by the grey-shaded region in Fig. 4 and shown in Fig. 5.

Moreover, winter time series of E_{INT} (Fig. 4c and 5c) and E_{EXT} (Fig. 4b and 5b) also follow tidal trends where prominent deviations in E_{INT} and E_{EXT} from the tidal trend are clearly distinguishable. These deviations are marked by downward spikes in E_{INT} and upward spikes in E_{EXT} (indicative of negatively- and positively-biased voltages, respectively). Like the greatest $\Delta pH^{INT-EXT}$ anomalies (Fig. 4a/5a), voltage spikes occur with the largest positive dSalt/dt (Fig. 4d/5d) on the flood tide and from starting slack ebb tide salinities of 1 after tide reversal (indicated by vertical red lines in Fig. 5). Coincidentally, downward spikes in E_{INT} and the greatest $\Delta pH^{INT-EXT}$ anomalies also occur when in situ temperature decreases at some of the largest negative dT/dt (\geq -1°C (0.5 h) $^{-1}$; Fig. 4e and 5e) on the flood tide after tide reversal.

In contrast, while $\Delta pH^{INT-EXT}$ anomalies follow the same asymmetric trends in summer, the range of observed $\Delta pH^{INT-EXT}$ anomalies (Fig. 6a) is substantially lower over narrower ranges of higher temperatures (Fig. 6d) and salinities (Fig. 6b) that remain >25°C and >15,

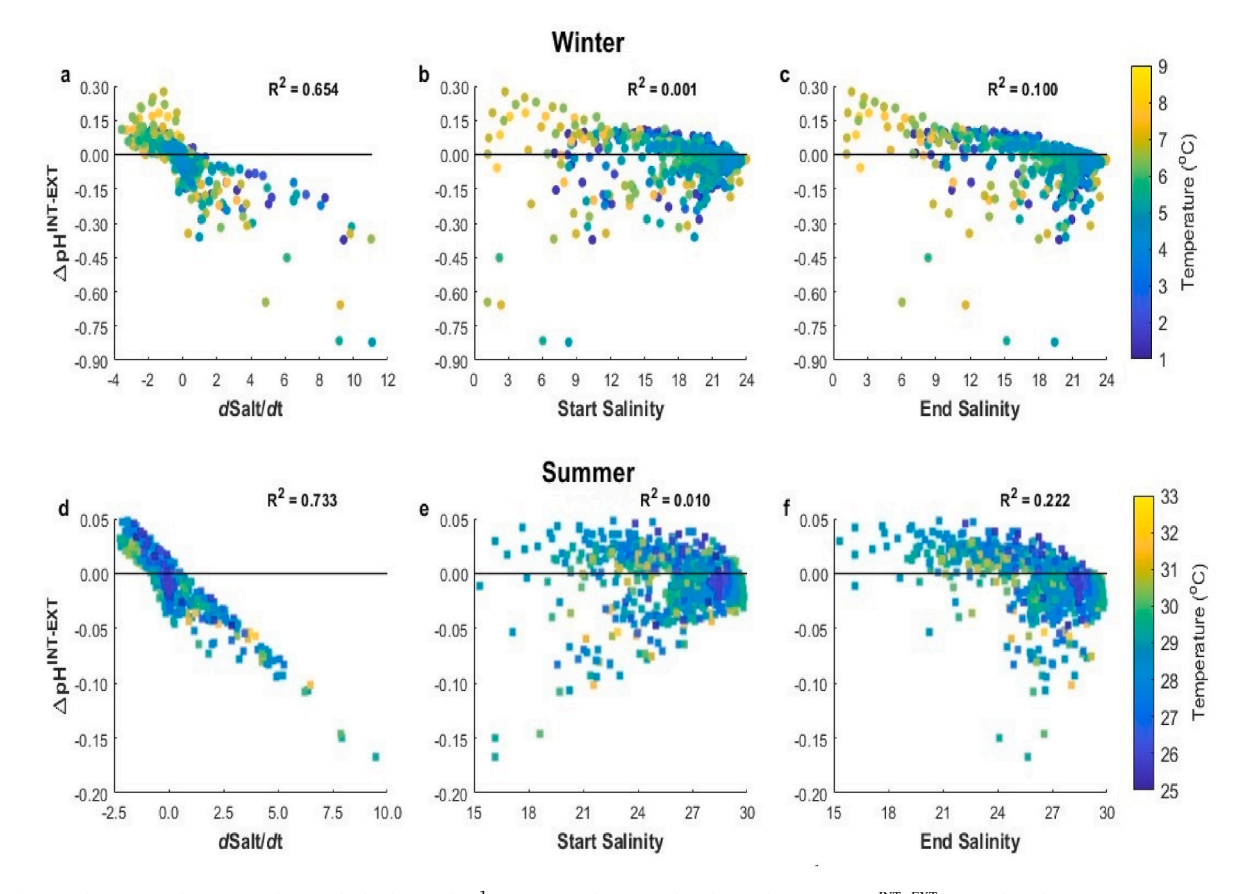


Fig. 8. Effect of the rate of change in salinity (dSalt/dt, (0.5 h)⁻¹), starting salinity, and ending salinity on $\Delta pH^{INT-EXT}$ anomalies during (a–c) winter 2016 between 27 January 2016 and 10 February 2016 (circles) and (d–f) summer between 20 July 2016 and 24 August 2016 (squares) as a function of end temperature (color-coded). Solid black lines correspond to a zero anomaly. Please note the different color bar scales of each set of panels. Start and end salinities represent the initial and final salinities for each time step recorded by the SBE37 conductivity-temperature sensor on the previous and current sampling cycles, respectively, performed every 30 min. dSalt/dt is the difference between them. (For interpretation of the references to color in this figure legend, the reader is referred to the Web version of this article.)

Table 1 Summary statistics for temperature, dT/dt, salinity, dSalt/dt, and pre- and post-correction $\Delta pH^{INT-EXT}$ anomalies.

Time Period	Parameter	n	Mean	Std Dev.	Min	Max
27 January 2016 to 10 February 2016	Temperature (°C)	656	4.561	1.684	1.343	8.169
	dT/dt (°C (0.5 h) ⁻¹)	656	0.00288	0.143	-1.111	0.892
	Salinity	656	18.831	4.947	1.170	23.974
	dSalt/ d t ((0.5 h) ⁻¹)	656	0.00312	1.751	-3.546	11.089
	Pre-Correction ΔpH ^{INT-EXT} Anomalies	656	-0.0245	0.101	-0.821	0.275
	Post-Correction $\Delta pH^{INT-EXT}$ Anomalies	656	-0.00718	0.0561	-0.459	0.117
20 July 2016 to 24 August 2016	Temperature (°C)	1612	28.872	1.213	25.429	32.274
	dT/dt (°C (0.5 h) ⁻¹)	1612	-0.00401	0.166	-1.463	1.528
	Salinity	1612	26.979	2.210	15.330	29.821
	dSalt/ d t ((0.5 h) ⁻¹)	1612	0.00206	0.955	-2.224	9.497
	Pre-Correction ΔpH ^{INT-EXT} Anomalies	1612	-0.00783	0.0199	-0.168	0.0476
	Post-Correction $\Delta pH^{INT-EXT}$ Anomalies	1612	-0.00443	0.0104	-0.0377	0.0294

respectively. Further, spikiness is also absent in summer time series of $E_{\rm INT}$ and $E_{\rm EXT}$ (data not shown) over $d{\rm Salt}/dt$ (Fig. 6c) and $d{\rm T}/dt$ (Fig. 6e) comparable to those observed during winter. Accordingly, reference electrode response appears to improve in summer.

3.2.2. Decoupling salinity and temperature effects on $\Delta p H^{\rm INT-EXT}$ anomalies

 $\Delta p H^{INT-EXT}$ anomalies were more poorly correlated with temperature (R $^2 \leq 0.020$) than with dT/dt (R $^2 < 0.1$) (winter – Fig. 7a–c; summer – Fig. 7d–f). So, neither temperature nor dT/dt have a consistent substantial effect on the $\Delta p H^{INT-EXT}$ anomalies. In contrast, $\Delta p H^{INT-EXT}$

anomalies generally exhibit better agreement with salinity ($R^2 \leq 0.222$) (winter - Fig. 8b and 8c; summer - Fig. 8e and 8f) over dT/dt and temperature. Clear linear relationships with the highest correlations emerge between $\Delta pH^{INT-EXT}$ anomalies and dSalt/dt (winter - Fig. 8a; summer - Fig. 8d; R^2 between 0.654 and 0.733) over wide temperature and salinity ranges. Ranges of $\Delta pH^{INT-EXT}$ anomalies also grow as tidal salinity variability increases and when salinities descend below 20 in winter and vice versa in summer when salinities remain $\geq \! 15$. Therefore, dSalt/dt is the clear dominant driver of the large $\Delta pH^{INT-EXT}$ anomalies in our work and was the strongest limiting factor of reference electrode response.

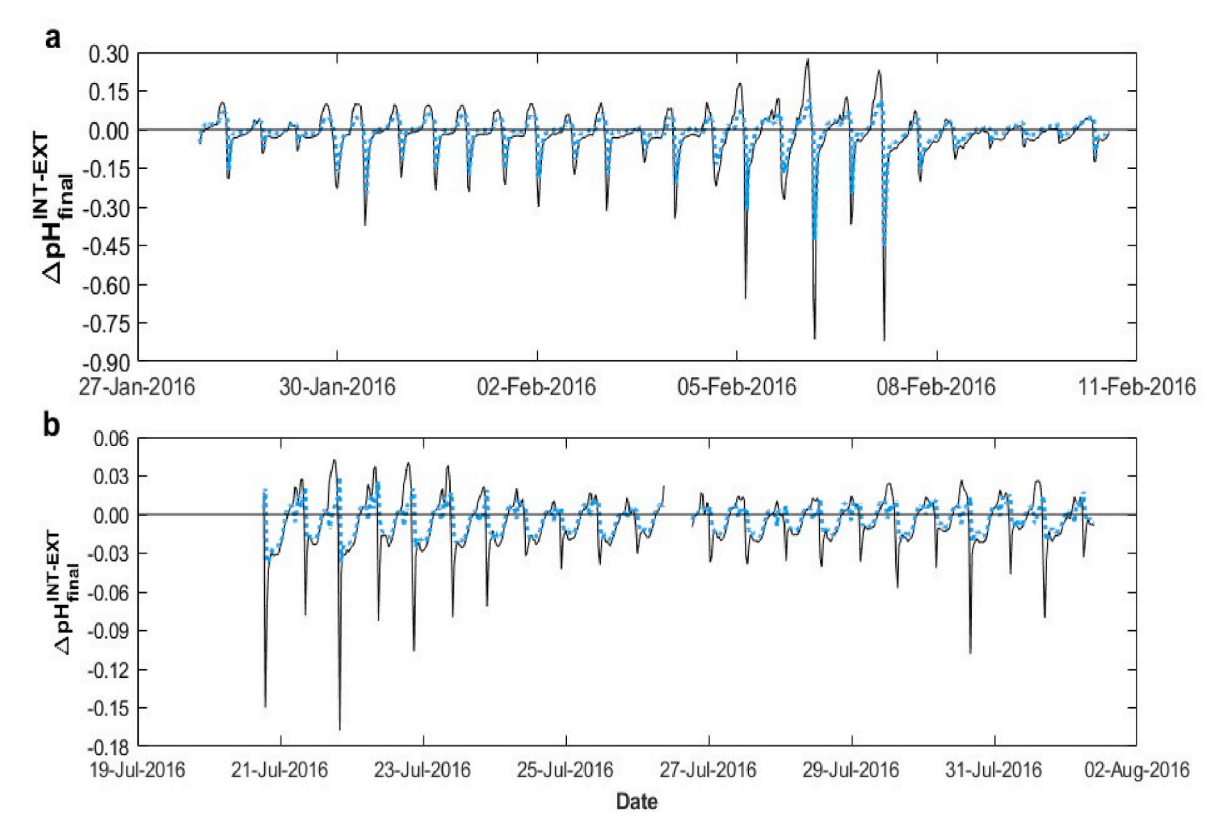


Fig. 9. Murderkill Estuary-Delaware Bay pH anomaly time-series from (a) winter between 27 January 2016 and 10 February 2016 and (b) summer between 20 July 2016 and 01 August 2016 before (solid black) and after (dotted sky blue) the dynamic sensor response correction for the Cl-ISE is applied relative to a zero anomaly. Gaps in the data in panel (b) represent sensor maintenance and proceeding 6-h intra-deployment conditioning periods. (For interpretation of the references to color in this figure legend, the reader is referred to the Web version of this article.)

It is important to note, though, that downward spikes in $E_{\rm INT}$ occur simultaneously with large negative dT/dt so dT/dt will still influence reference electrode response. Though, dT/dt will influence sensor response to a lesser extent compared to dSalt/dt since salinity variability tied to tidal cycles is larger relative to temperature variability. Taken together with the observed spikes in $E_{\rm INT}$ and $E_{\rm EXT}$ that coincide with the greatest $\Delta pH^{\rm INT-EXT}$ anomalies, each reference electrode exhibits dynamic errors in their temperature and/or salinity responses over rapidly changing environmental conditions. Therefore, the large $\Delta pH^{\rm INT-EXT}$ anomalies are a composite result of dynamic errors in both $pH^{\rm INT}$ and $pH^{\rm EXT}$.

3.2.3. Applying the dynamic sensor response correction

A >40% reduction in tidally-driven winter $\Delta pH^{INT-EXT}$ anomaly ranges is achieved (Table 1/Fig. 9a) once E_{EXT}^{corr} is applied. Although, substantial $\Delta pH^{INT-EXT}$ anomalies >±0.4 pH still remain in winter. If the application of E_{EXT}^{corr} reduces errors in pHEXT resulting from the dynamic temperature and salinity responses of the Cl-ISE, then we must also inevitably assume some portion of the $\Delta pH^{INT-EXT}$ anomaly that remains after processing raw sensor data using the reference pH from validation samples can be attributed, at least in part, to dynamic temperature and salinity responses of the Ag/AgCl internal reference.

The impacts of applying E_{EXT}^{corr} are even more prominent in summer (Table 1/Fig. 9b) as pH^{INT} and pH^{EXT} approach parity and the Δ $pH^{INT-EXT}$ anomaly range is reduced by 68.7% to $<\pm 0.04$ pH. Despite these reductions, their asymmetric tidal trends endure. Most importantly, the application of E_{EXT}^{corr} removes the first order salinity dependence of the $\Delta pH^{INT-EXT}$ anomalies for all data with post-correction relationships between $\Delta pH^{INT-EXT}$ anomalies and dSalt/dt (Fig. S5) exhibiting R^2 between 0.002 and 0.172. Further, since temperature is

used to calculate $\gamma_H \gamma_{CI}$ from Khoo et al. (1977), E_{EXT}^{corr} also incorporates a dynamic temperature correction to help account for dT/dt; although post-correction correlations between $\Delta pH^{INT-EXT}$ anomalies and dT/dt did not exhibit any substantial changes (data not shown). For further discussion of the impacts of the Cl-ISE dynamic sensor response correction, please see the Supplementary Materials.

3.3. Limits of assessement

It must be noted that the data presented here were collected using only one sensor in a system that experiences simultaneous substantial temperature and salinity variability. Further, in situ $\Delta p H^{INT-EXT}$ anomalies will also vary based on user-defined sensor deployment configurations (i.e., pump times and pH sample averages) and be subject to inter-sensor variability (Bresnahan et al., 2014; Martz et al., 2010). The winter $\Delta p H^{INT-EXT}$ anomalies reported here represent some of the most extreme values yet observed. The winter anomalies were specifically used for the purposes of our assessment and winter pH should not be used in further biogeochemical contexts.

4. Conclusions

Empirical assessments of reference electrode response conducted over wide ranges of temperature, dT/dt, salinity, and dSalt/dt revealed that dSalt/dt was the strongest limiting factor of reference electrode response and tidally driven $\Delta pH^{INT-EXT}$ anomalies were a composite result of dynamic response issues of both reference electrodes. Therefore, dynamic errors in reference electrode response can no longer be ignored and must be considered in future experimental designs. While the dynamic sensor response correction for the Cl-ISE works for our specific application and sampling interval, additional work is still

needed before it is ready for widespread implementation. At this time, the correction is also not suitable for sensor applications where pressure sensitivity must be accounted for (e.g., profiling using the Deep-Sea Durafet – Johnson et al. (2016)).

Moreover, additional work is needed to develop an independent dynamic sensor response correction for the internal reference electrode to address dynamic errors that could be imparted into pH^{INT} because of liquid junction potentials and thermal lags in the internal saturated KCl gel. Several researchers have reported successful deployments of Durafet-based biogeochemical sensors over our winter temperature range in seawater at salinity >34 (Kapsenberg et al., 2015; Matson et al., 2011). However, based on our analyses, reference electrode response at low temperatures over rapidly changing salinities between freshwater and seawater requires further study.

Based on our findings, there is an inherent need to address the role of $\Delta p H^{\rm INT-EXT}$ anomalies in sensor data quality control and data reporting in estuarine and other dynamic applications beyond the simple detection of biofouling and sensor malfunction. First, acceptable $\Delta p H^{\rm INT-EXT}$ anomaly threshold ranges should be standardized. Second, what magnitude of $\Delta p H^{\rm INT-EXT}$ anomalies is acceptable in the context of other data quality metrics such as the accuracy of $p H^{\rm INT}$ and $p H^{\rm EXT}$ relative to the chosen reference also needs to be established. In the end, we hope this work stimulates further discussion around the role and treatment of large $\Delta p H^{\rm INT-EXT}$ anomalies and the dynamic errors in reference electrode response that drive them in the context of Sensor Best Practices for the benefit of the OA and sensor user communities.

CRediT authorship contribution statement

S. Fisher Gonski: Writing – review & editing, Writing – original draft, Visualization, Validation, Methodology, Investigation, Formal analysis, Data curation, Conceptualization. William J. Ullman: Writing – review & editing, Validation, Methodology, Investigation. D. Tye Pettay: Writing – review & editing, Validation, Investigation. Karl S. Booksh: Writing – review & editing, Validation, Investigation. Todd R. Martz: Writing – review & editing, Validation, Methodology, Investigation. George W. Luther, III: Validation, Investigation, Methodology, Supervision, Writing – review & editing. Wei-Jun Cai: Writing – review & editing, Validation, Supervision, Resources, Project administration, Methodology, Investigation, Funding acquisition, Conceptualization.

Declaration of competing interest

The authors declare that they have no known competing financial interests or personal relationships that could have appeared to influence the work reported in this paper.

Data availability

Data will be made available on request.

Acknowledgements

We sincerely thank Yuichiro Takeshita of Monterey Bay Aquarium Research Institute, Taylor Wirth of Scripps Institution of Oceanography, and Philip Bresnahan of University of North Carolina Wilmington for their insights and support. We thank the staff of University of Delaware's Lewes Campus Maintenance and Operations and University of Delaware's Marine Operations for their assistance with sensor modifications. Finally, we thank three anonymous reviewers for their helpful comments. Financial support for this work was provided by the National Science Foundation's EPSCoR (Grant No. 1757353) and the State of Delaware. Lillian Wong of the Delaware Geological Survey drafted Fig. 1.

Appendix A. Supplementary data

Supplementary data to this article can be found online at https://doi. org/10.1016/j.ecss.2023.108247.

References

- Bagshaw, E.A., Wadham, J.L., Tranter, M., Beaton, A.D., Hawkings, J.R., Lamarche-Gagnon, G., Mowlem, M.C., 2021. Measuring pH in low ionic strength glacial meltwaters using ion selective field effect transistor (ISFET) technology. Limnol Oceanogr. Methods 19 (3), 222–233.
- Bard, A.J., Parsons, R., Jordan, J., 1985. Standard Potentials in Aqueous Solutions, first ed. CRC Press.
- Bates, N.R., Astor, Y.M., Church, M.J., Currie, K., Dore, J.E., Gonzalez-Davila, M., Lorenzoni, L., Muller-Karger, F., Olafsson, J., Santana-Casiano, J.M., 2014. A time-series view of changing surface ocean chemistry due to ocean uptake of anthropogenic CO₂ and ocean acidification. Oceanography 27 (1), 126–141.
- Bates, R.G., 1973. Determination of pH: Theory and Practice, second ed. Wiley-Interscience.
- Baumann, H., Wallace, R.B., Tagliaferri, T., Gobler, C.J., 2015. Large natural pH, $\rm CO_2$ and $\rm O_2$ fluctuations in a temperate tidal salt marsh on diel, seasonal, and interannual time scales. Estuar. Coast 38 (1), 220–231.
- Bresnahan, P.J., Martz, T.R., Takeshita, Y., Johnson, K.S., LaShomb, M., 2014. Best practices for autonomous measurements of seawater pH with the Honeywell Durafet. Methods Oceanogr. 9, 44–60.
- Bresnahan, P.J., Takeshita, Y., Wirth, T., Martz, T.R., Cyronak, T., Albright, R., et al., 2021. Autonomous in situ calibration of ion-sensitive field effect transistor pH sensors. Limnol Oceanogr. Methods 19 (2), 132–144.
- Butler, R.A., Covington, A.K., Whitfield, M., 1985. The determination of pH in estuarine waters. II: Practical considerations. Oceanol. Acta 8 (4), 433–439.
- Cai, W.-J., Reimers, C.E., 1993. The development of pH and pCO₂ microelectrodes for studying the carbonate chemistry of pore waters near the sediment-water interface. Limnol. Oceanogr. 38 (3), 1762–1773.
- Carstensen, J., Duarte, C.M., 2019. Drivers of pH variability in coastal ecosystems. Environ. Sci. Technol. 53 (8), 4020–4029.
- Culberson, C.H., 1981. Direct potentiometry. In: Whitfield, M., Jagner, D. (Eds.), Marine Electrochemistry. Wiley, pp. 187–261.
- Dzwonkowski, B., Wong, K.-C., Ullman, W.J., 2013. Water level and velocity characteristics of a salt marsh channel in the Murderkill Estuary, Delaware. J. Coast Res. 30 (1), 63–74.
- Dickson, A.G., 1984. pH scales and proton-transfer reactions in saline media such as seawater. Geochem. Cosmochim. Acta 48 (11), 2299–2308.
- Dickson, A.G., Camoes, M.F., Spitzer, P., Fisicaro, P., Stoica, D., Pawlowicz, R., Feistel, R., 2016. Metrological challenges for measurements of key climatological observables. Part 3: seawater pH. Metrologia 53 (1), R26.
- Dickson, A.G., Sabine, C.L., Christian, J.R., 2007. Guide to Best Practices for Ocean CO₂

 Measurements.
- Duke, P.J., Else, B.G.T., Jones, S.F., Marriot, S., Ahmed, M.M.M., Nandan, V., et al., 2021. Seasonal marine carbon system processes in an Arctic coastal landfast ice environment observed with an innovative sensor platform. Elementa: Sci. Anthropocene 9 (1).
- Easley, R.A., Byrne, R.H., 2012. Spectrophotometric calibration of pH electrodes in seawater using purified m-cresol purple. Environ. Sci. Technol. 46 (9), 5018–5024.
- Evans, W., Pocock, K., Hare, A., Weekes, C., Hales, B., Jackson, J., et al., 2019. Marine CO₂ patterns in the northern salish sea. Front. Mar. Sci. 5, 536.
- Fritzsche, E., Staudinger, C., Fischer, J.P., Thar, R., Jannasch, H.W., Plant, J.N., et al., 2018. A validation and comparison study of new, compact, versatile optodes for oxygen, pH and carbon dioxide in marine environments. Mar. Chem. 207, 63–76.
- Gonski, S.F., Cai, W.-J., Ullman, W.J., Joesoef, A., Main, C.R., Pettay, D.T., Martz, T.R., 2018. Assessment of the suitability of Durafet-based sensors for pH measurement in dynamic estuarine environments. Estuar. Coast Shelf Sci. 200, 152–168.
- Hofmann, G.E., Smith, J.E., Johnson, K.S., Send, U., Levin, L.A., Micheli, F., et al., 2011. High-frequency dynamics of ocean pH: a multi-ecosystem comparison. PLoS One 6 (12), e28983.
- Johnson, K.S., Jannasch, H.W., Coletti, L.J., Elrod, V.A., Martz, T.R., Takeshita, Y., Carlson, R.J., Connery, J.G., 2016. Deep-Sea DuraFET: a pressure tolerant pH sensor designed for global sensor networks. Anal. Chem. 88 (6), 3249–3256.
- Kapsenberg, L., Kelley, A.L., Shaw, E.C., Martz, T.R., Hofmann, G.E., 2015. Near-shore Antarctic pH variability has implications for the design of ocean acidification experiments. Sci. Rep. 5, 9638.
- Khoo, K.H., Ramette, R.W., Culberson, C.H., Bates, R.G., 1977. Determination of hydrogen ion concentrations in seawater from 5 to 40°C: standard potentials at salinities from 20 to 45. Anal. Chem. 49 (1), 29–34.
- Long, M.H., 2021. Aquatic biogeochemical eddy covariance fluxes in the presence of waves. J. Geophys. Res.: Oceans 126 (2), e2020JC016637.
- Martell-Bonet, L., Byrne, R.H., 2020. Characterization of the nonlinear salinity dependence of glass pH electrodes: a simplified spectrophotometric calibration procedure for potentiometric seawater pH measurements at 25° C in marine and brackish waters: $0.5 \le S \le 36$. Mar. Chem. 220, 103764.
- Martz, T., 2015. SeaFET & SeapHOx Users Guide. Scripps Institute of Oceanography, San Diego. Version 3. University of California.
- Martz, T.R., Connery, J.G., Johnson, K.S., 2010. Testing the Honeywell Durafet for seawater pH applications. Limnol Oceanogr. Methods 8, 172–184.

- Martz, T.R., Daly, K.L., Byrne, R.H., Stillman, J.H., Turk, D., 2015. Technology for ocean acidification research: needs and availability. Oceanography 28 (2), 40–47.
- Matson, P.G., Martz, T.R., Hofmann, G.E., 2011. High-frequency observations under Antarctic sea ice in the southern Ross Sea. Antarct. Sci. 23, 607–613, 06.
- Miller, C.A., Bonsell, C., McTigue, N.D., Kelley, A.L., 2021. The seasonal phases of an Arctic lagoon reveal the discontinuities of pH variability and CO₂ flux at the air–sea interface. Biogeosciences 18 (3), 1203–1221.
- Miller, C.A., Kelley, A.L., 2021. Seasonality and biological forcing modify the diel frequency of nearshore pH extremes in a subarctic Alaskan estuary. Limnol. Oceanogr. 2021, 1–17.
- Miller, C.A., Pocock, K., Evans, W., Kelley, K.L., 2018. An evaluation of the performance of Sea-Bird Scientific's SeaFET autonomous pH sensor: considerations for the broader oceanographic community. Ocean Sci. 14, 751–768.
- Millero, F.J., 1986. The pH of estuarine waters. Limnol. Oceanogr. 31 (4), 839–847. O'Boyle, S., McDermott, G., Noklegaard, T., Wilkes, R., 2013. A simple index of trophic
- O'Boyle, S., McDermott, G., Noklegaard, T., Wilkes, R., 2013. A simple index of trophic status in estuaries and coastal bays based on measurements of pH and dissolved oxygen. Estuar. Coast 36 (1), 158–173.
- Oldham, K., Myland, J., Bond, A., 2011. Electrochemical Science and Technology: Fundamentals and Applications. John Wiley & Sons.
- Pettay, D.T., Gonski, S.F., Cai, W.J., Sommerfield, C.K., Ullman, W.J., 2020. The ebb and flow of protons: a novel approach for the assessment of estuarine and coastal acidification. Estuar. Coast Shelf Sci. 236, 106627.
- Provoost, P., Van Heuven, S., Soetaert, K., Laane, R.W.P.M., Middelburg, J.J., 2010. Seasonal and long-term changes in pH in the Dutch coastal zone. Biogeosciences 7 (11), 3869.

- Rivest, E.B., O'Brien, M., Kapsenberg, L., Gotschalk, C.C., Blanchette, C.A., Hoshijima, U., Hofmann, G.E., 2016. Beyond the benchtop and the benthos: dataset management planning and design for time series of ocean carbonate chemistry associated with Durafet-based pH sensors. Ecol. Inf. 36, 209–220.
- Shangguan, Q., Prody, A., Wirth, T.S., Briggs, E.M., Martz, T.R., DeGrandpre, M.D., 2022. An inter-comparison of autonomous in situ instruments for ocean CO₂ measurements under laboratory-controlled conditions. Mar. Chem. 240, 104085.
- Takeshita, Y., Johnson, K.S., Martz, T.R., Plant, J.N., Sarmiento, J.L., 2018. Assessment of autonomous pH measurements for determining surface seawater partial pressure of CO₂. J. Geophys. Res.: Oceans 123 (6), 4003–4013.
- Takeshita, Y., Martz, T.R., Johnson, K.S., Dickson, A.G., 2014. Characterization of an ion-selective field effect transistor and chloride ion-selective electrodes for pH measurements in seawater. Anal. Chem. 86 (22), 1189–1195.
- Ullman, W.J., Aufdenkampe, A., Hays, R.L., Dix, S., 2013. Nutrient Exchange between a Salt Marsh and the Murderkill Estuary, Kent County, Delaware. Part C. Technical Report. Delaware Department of Natural Resources and Environmental Control, Dover, DE (unpublished).
- Voynova, Y.G., Lebaron, K.C., Barnes, R.T., Ullman, W.J., 2015. *In situ* response of bay productivity to nutrient loading from a small tributary: the Delaware Bay-Murderkill Estuary tidally-coupled biogeochemical reactor. Estuar. Coast Shelf Sci. 160, 33–48.
- Whitfield, M., Butler, R.A., Covington, A.K., 1985. The determination of pH in estuarine waters. I: definition of pH scales and selection of buffers. Oceanol. Acta 8 (4), 423–432
- Wong, K.C., Dzwonkowski, B., Ullman, W.J., 2009. Temporal and spatial variability of sea level and volume flux in the Murderkill Estuary. Estuar. Coast Shelf Sci. 84, 440–446